

Computational Materials Science II

BAND STRUCTURE AND DENSITY OF STATES OF 2D TRANSITION METAL DICHALCOGENIDES

Vourvachakis S. Georgios

mse354

May 23, 2025



This work is licensed under a [Creative Commons “Attribution-NonCommercial-NoDerivatives 4.0 International” license](#).



CONTENTS

1	Introduction	3
1.1	Structural Phases of 2D TMDs	3
1.2	Electronic Structure Theory (DFT, Bloch Bands, and DOS)	6
1.3	GGA-PBE Functional and Its Implementation in GPAW	8
1.3.1	Sketch Proof of the Enhancement Factor	8
1.3.2	Correction to LDA	9
1.3.3	PBE in GPAW	9
1.4	Computational Approach	9
2	Crystal Structures and Lattice Setup	10
3	Computational Parameters and Relaxation	11
4	Ground-State Calculations (DFT+U and SOC)	12
5	Band Structure Calculations	12
6	Density of States and Projections	13
7	Parallelization and Computation	14
8	Workflow for $\text{1T}'\text{-WTe}_2$ Calculations	15
9	Results and Remarks	16
9.1	Band Gap Accuracy and Trends	25
10	Environment Setup	25
10.1	Adjusting the Path Settings	27

I INTRODUCTION

Following the isolation of graphene in 2004, the search for atomically thin materials with intrinsic band gaps has become a major theme in condensed matter physics [1]. Among these, two-dimensional transition-metal dichalcogenides (2D TMDs) of the type MX_2 (M a transition metal such as Mo or W, X a chalcogen S, Se or Te) have emerged as prototypical semiconductors. In particular, group-VI TMD monolayers (MoS_2 , MoSe_2 , MoTe_2 , WS_2 , WSe_2 , WTe_2) combine atomic-scale thickness, direct optical band gaps, and strong spin-orbit coupling (SOC), making them attractive for nanoelectronics, optoelectronics, valleytronics, and studies of novel phases [2]. Bulk MoS_2 , for example, is an indirect-gap semiconductor, but its exfoliated monolayer exhibits a direct gap of order ~ 1.8 eV [3]. This and related materials have been intensively studied experimentally (e.g. MoS_2 field-effect transistors [4]) and theoretically as a rich playground for reduced-dimensional physics [5].

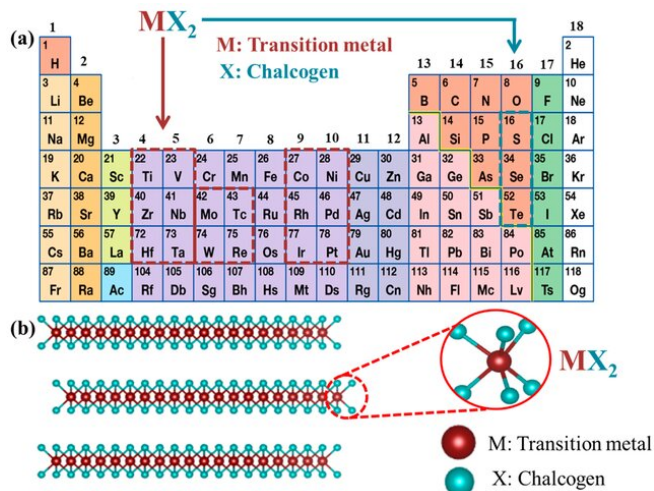


Figure 1: (a) TMDs with the MX_2 structure consisting of M from the 16 transition metals indicated by the red dotted box and X from the three halogen elements indicated by the green dotted box, (b) layered structure of MX_2 .[6]

I.I STRUCTURAL PHASES OF 2D TMDs

Group-VI TMD monolayers exhibit several polymorphic crystal structures. The most common is the trigonal-prismatic (iH or “ 2H -type” stacking) structure, in which each metal atom is coordinated by six chalcogens in a prismatic geometry (point group D_{3h}). In contrast, the iT polytype has an octahedral (or trigonal antiprismatic, D_{3d}) coordination around the metal. For example, bulk MoS_2 can form 2H (ABA) or iT (ABC) stackings, but a single layer occurs only in the 2H (iH monolayer) or iT phase. The iH and iT structures are illustrated schematically in Fig.2. Finally, the iT' (distorted iT) phase breaks the symmetry further: in mono-

layer WTe₂ (and MoTe₂), the rT' distortion consists of zigzag chains of metal atoms and a slight monoclinic distortion of the lattice, lowering the point group (Fig. 2(C)). Experimentally, some TMDs such as TaS₂ in the rT polytype undergo further charge-density-wave (C-CDW) distortions, e.g. the infamous “star-of-David” 13-atom cluster seen in rT-TaS_2 .

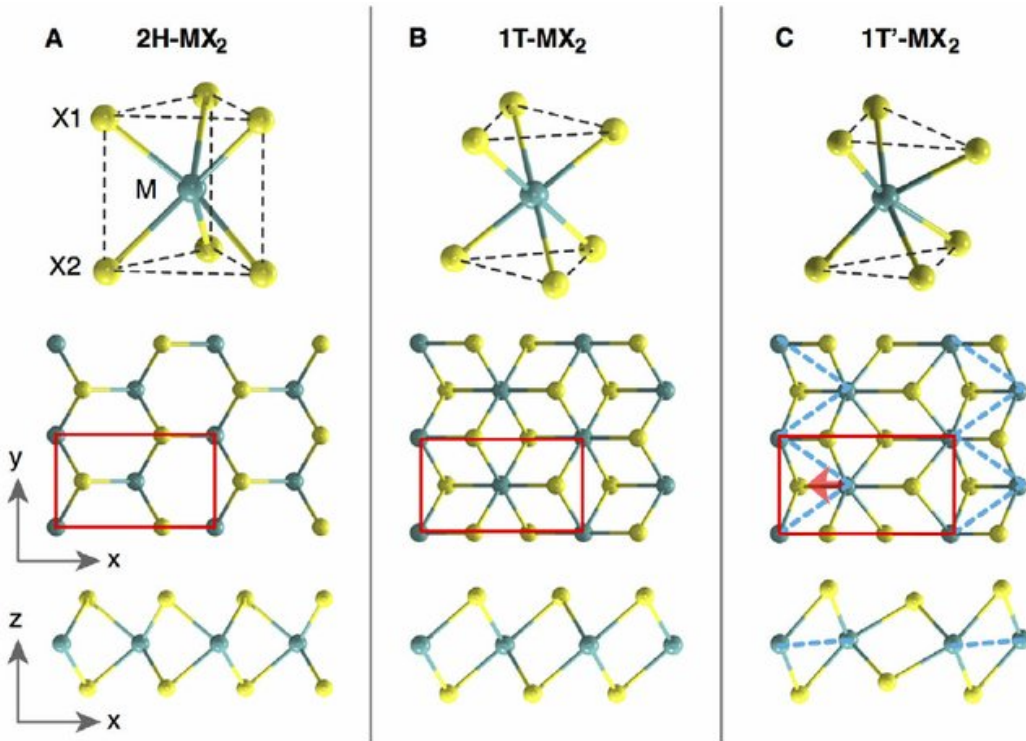


Figure 2: Atomistic structure of monolayer TMD. (A) 2H-MX₂ where M atoms are trigonal-prismatically coordinated by six X atoms, forming ABA stacking with the P6m₂ space-group. (B) rT-MX₂ where M atoms are octahedrally coordinated with the nearby six X atoms, forming ABC stacking with the P3m₁ space group. (C) rT'-MX₂, distorted rT-MX₂, where the distorted M atoms form one-dimensional zigzag chains indicated by the dashed blue line. Their unit cell is indicated by red rectangles.[7]

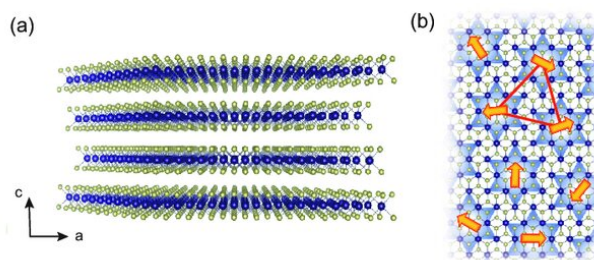


Figure 3: (a) Crystal structure of rT-TaS_2 . Each layer consists of tantalum atoms (blue) sandwiched by sulfur atoms (yellow). (b) A schematics of the star-of-David clusters, which appear as a result of the C-CDW transition. In the Mott insulating state, the electrons localized at the centers of the clusters form $S = 1/2$ 2D perfect triangular lattice.[8]

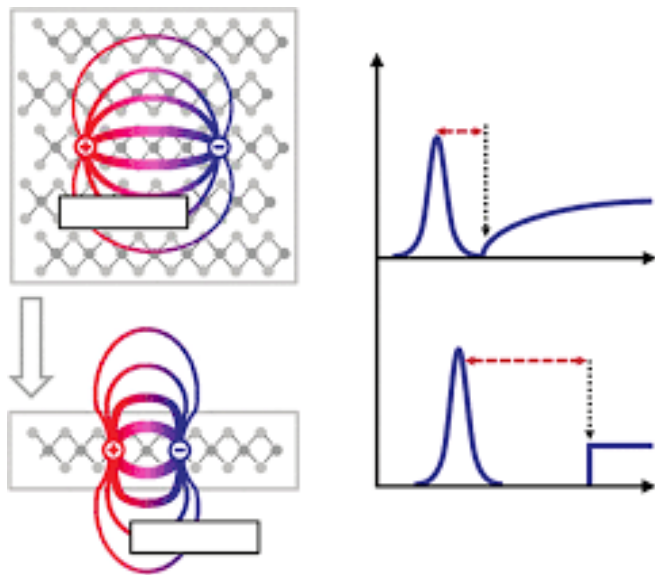


Figure 4: (a) Real-space representation of excitons in three-dimensional and two-dimensional systems. The changes in the dielectric environment are schematically represented by the respective dielectric constants ϵ_{3D} and ϵ_{2D} and the permittivity of free space ϵ_0 . (b) The effects of dimensionality on the electronic and excitonic properties schematically represented by the optical absorption spectra. Change in dimensionality from 3D to 2D leads to an increase in the band gap and exciton binding energy represented by red dashed line.[9]

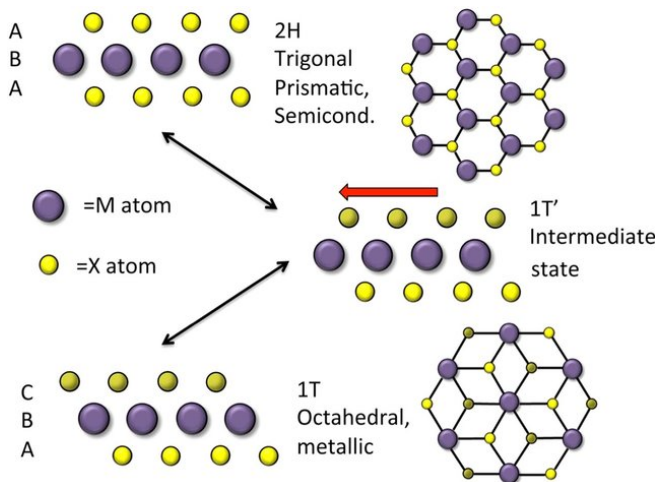


Figure 5: Model of the 2H-1T phase transition in MoX_2 films. The 2H phase is trigonal prismatic and the material is a semiconductor. The 1T phase is octahedral and the material is metallic. The 1T' phase is an intermediate state.[10]

The different geometries lead to markedly different electronic properties. The trigonal-prismatic 1H phases of MoS_2 , MoSe_2 , WS_2 , and WSe_2 are well-known semiconductors with sizable band gaps. In contrast, the octahedral 1T phases tend to be metallic: e.g. in MoS_2 the 1T polymorph is metallic whereas the 1H form is semiconducting [10]. The distorted 1T' phases often exhibit semi-metallic or topological behavior.

For instance, monolayer WTe₂ in the iT' structure has been predicted and recently observed to realize a two-dimensional quantum spin Hall insulator (a topological semimetallic phase) under appropriate conditions. Likewise, bulk iT'-MoTe₂ is a type-II Weyl semimetal (see Fig. 6), and its monolayer also has a small indirect band overlap. Thus, by phase-engineering (e.g. via strain, doping or substrate effects) one can tune group-VI TMDs from semiconductors into metals or topological semimetals [11].

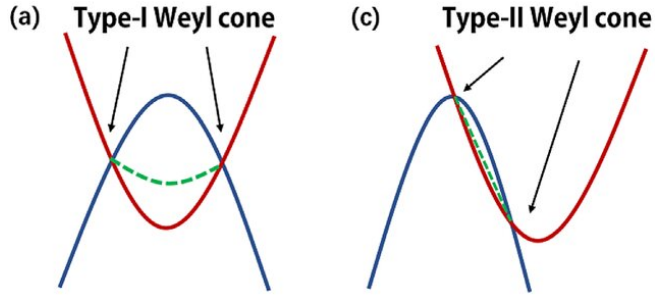


Figure 6: Type-I and type-II Weyl semimetals (a) A sketch of the e-k dispersion of a type-I Weyl semimetal which can be viewed as a negative direct bandgap semiconductor. The type-I Weyl nodes exist at the crossing points where the conduction band (red) and valence band (blue) dip into each other. A Fermi arc (green dotted line) connects the pair of Weyl nodes. (b) The Fermi surface (Fs) on the surface of a type-I Weyl semimetal as depicted in (a). The Fermi level is located at the energy of the Weyl nodes. Bulk Weyl cones are projected onto the surface as two discrete points (red, blue) connected by a Fermi arc surface state (dotted green line).[12]

I.2 ELECTRONIC STRUCTURE THEORY (DFT, BLOCH BANDS, AND DOS)

To understand and predict these behaviors, we employ *density functional theory* (DFT) to calculate electronic band structures and densities of states (DOS) [13]. DFT is based on the Hohenberg–Kohn theorems, which guarantee that the ground-state energy is a functional of the electron density $n(\mathbf{r})$ [14],[15]. In practice one solves the Kohn–Sham equations for a fictitious non-interacting electron system under an effective potential.

In atomic units the Kohn–Sham equations read

$$\left[-\frac{1}{2} \nabla^2 + V_{\text{ext}}(\mathbf{r}) + V_H[n](\mathbf{r}) + V_{xc}[n](\mathbf{r}) \right] \phi_i(\mathbf{r}) = \epsilon_i \phi_i(\mathbf{r})$$

where the effective potential includes the external (nuclear) potential, the Hartree (Coulomb) potential $V_H[n]$, and the exchange-correlation potential $V_{xc}[n] = \partial E_{xc}[n]/\partial n$.

The Kohn–Sham orbitals $\phi_i(\mathbf{r})$ yield the ground-state density $n(\mathbf{r}) = \sum_i |\phi_i|^2$. Bloch's theorem applies because the monolayer crystals have 2D periodicity: each electronic state can be written as $\psi_{n\mathbf{k}}(\mathbf{r}) = e^{i\mathbf{k}\cdot\mathbf{r}} u_{n\mathbf{k}}(\mathbf{r})$, with $u_{n\mathbf{k}}(\mathbf{r})$ lattice-periodic and \mathbf{k} the 2D crystal momentum [16].

One then obtains energy bands $E_n(\mathbf{k})$ by solving the Kohn–Sham equations for each \mathbf{k} -point in a high-symmetry path through the 2D Brillouin zone (for hexagonal lattices one typically goes $\Gamma - K - M - \Gamma$).

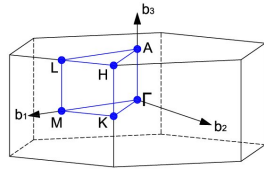


Figure 7: High symmetry path in the hexagonal Brillouin zone chosen according to the notation of [17].

The total density of states (DOS) is computed from the band energies over the Brillouin zone, and provides a complementary view of the spectrum. In our study we will focus on the *electronic band structures* $E_n(\mathbf{k})$ and the *DOS of each phase*.

To gain insight into the atomic character of the electronic states, we also analyze the *orbital-projected (or partial) density of states (PDOS)*. This involves projecting the Kohn–Sham eigenstates onto atomic orbital channels (e.g. metal d or chalcogen p). In the group-VI 1H TMDs, for example, it is well-known that the valence-band edge derives primarily from the chalcogen p orbitals (hybridized with metal d), whereas the conduction-band edge is mainly metal d -like (e.g., see Fig. 8). An orbital PDOS plot thus helps identify which atomic species and orbitals contribute to bands near the Fermi level. Tracking these contributions is especially important when comparing different materials (S vs Se vs Te) or phases, since subtle hybridizations can shift band positions. In our work we will compute the total DOS and metal- d /chalcogen- p PDOS for each material and phase, facilitating a direct assignment of orbital character to features in the spectrum.

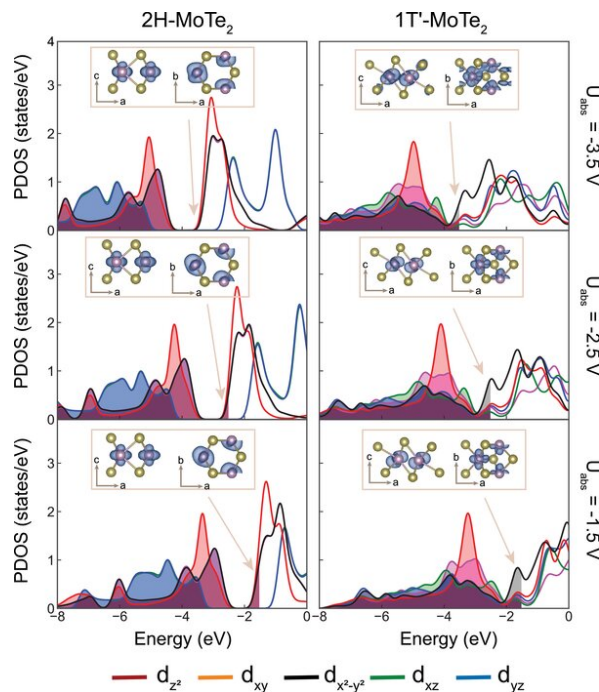


Figure 8: The d-orbital projected density of states (PDOS) of 2H- and 1T' - MoTe₂ under different potentials. The shadows represent occupied states. The insets are side and top views of the corresponding spatial charge densities in the highest occupied states. The vacuum energy levels are set to zero.[18]

I.3 GGA-PBE FUNCTIONAL AND ITS IMPLEMENTATION IN GPAW

The Generalized Gradient Approximation (GGA) proposed by Perdew, Burke, and Ernzerhof in 1996 provides an improvement over the Local Density Approximation (LDA) by including *first-order density gradient corrections* to the exchange-correlation (xc) energy. The PBE functional is defined by an *enhancement factor* that modulates the LDA exchange energy density, yielding

$$E_x^{\text{PBE}}[n] = \int d\mathbf{r} \epsilon_x^{\text{LDA}}(n) F_x(s),$$

where

$$F_x(s) = 1 + \kappa - \frac{\kappa}{1 + \mu s^2 / \kappa}$$

with the reduced gradient

$$s(\mathbf{r}) = \frac{|\nabla_{\mathbf{r}} n|}{2k_F n}, \quad k_F^{(3D)} = (3\pi^2 n)^{1/3},$$

and constants and chosen to satisfy known exact constraints and to recover the correct second-order gradient expansion in the slowly varying limit [19].

I.3.1 Sketch Proof of the Enhancement Factor

The PBE enhancement factor is constructed by enforcing:

- 1. **Uniform electron gas limit:** $F_x(0) = 1$, so that for constant density, PBE reduces to LDA exchange.
- 2. **Second-order gradient expansion:** In the limit of small s , the expansion

$$F_x(s) \approx 1 + \mu s^2 + \mathcal{O}(s^4)$$

must reproduce the known exchange gradient coefficient from perturbation theory.

- 3. **Lieb–Oxford bound:** For large s , $F_x(s)$ must not exceed a finite constant to respect the lower bound on the xc energy. This yields the asymptotic plateau at $1 + \kappa$.

By choosing the denominator $1 + \mu s^2 / \kappa$, one constructs the minimal analytic form that interpolates between these limits. Expanding for small s gives:

$$F_x(s) = 1 + \kappa - \kappa \left(1 - \frac{\mu}{\kappa} s^2 + \mathcal{O}(s^4) \right) = 1 + \mu s^2 + \mathcal{O}(s^4),$$

recovering the gradient expansion coefficient μ . At large the factor saturates at $1 + \kappa$, thus respecting the Lieb–Oxford bound [20].

1.3.2 Correction to LDA

While LDA employs a purely local exchange energy density

$$\epsilon_s^{\text{LDA}}(n) = -\frac{3}{4} \left(\frac{3}{\pi}\right)^{1/3} n^{4/3},$$

it neglects density inhomogeneity. PBE adds a positive correction for regions of varying density through the enhancement factor, which reduces self-interaction errors and improves binding energies, surface energies, and barrier heights in molecular systems [19],[20].

1.3.3 PBE in GPAW

The real-space, projector-augmented wave (PAW) code GPAW implements the PBE functional by calling the `Libxc` library, which provides the analytic forms of the energy density and its functional derivatives. In practice, at each grid point GPAW evaluates:

1. The local density $n(\mathbf{r})$ and its gradient ∇n .
2. The reduced gradient $s(\mathbf{r})$.
3. The enhancement factor $F_x(s)$ and its derivatives with respect to n and ∇n .
4. The exchange potential components for self-consistent field iterations.

Internally, GPAW uses the following pseudocode structure (adapted from Mortensen et al. 2005):

```
for each grid point r:
    n = density[r]
    grad_n = gradient(density)[r]
    s = |grad_n| / (2 * (3 * pi^2 * n)^(1/3) * n)
    Fx = 1 + kappa - kappa / (1 + mu * s^2 / kappa)
    eps_x = eps_x_LDA(n) * Fx
    compute derivatives: dFx_dn, dFx_dgrad_n
    accumulate exchange energy and potential contributions
```

This implementation yields computational efficiency by avoiding higher-order gradient evaluations, while maintaining accuracy across a variety of materials systems [21].

I.4 COMPUTATIONAL APPROACH

The electronic structure calculations are performed using the `GPAW` package, a real-space projector-augmented-wave code, together with the `Atomic Simulation Environment (ASE)` for structure generation. A detailed methodological description is given in Sec. II in [17]; here we only note the key ingredients. GPAW solves the Kohn–Sham equations (eq.1.2) on a real-space grid, enabling straightforward treatment of 2D materials with periodic boundary conditions. ASE provides a flexible Python interface to build the monolayer geometries

($\text{iH}-\text{MX}_2$, $\text{iT}-\text{WTe}_2$, $\text{iT}'-\text{WTe}_2$) and to automate convergence tests. We use exchange-correlation functionals of the generalized-gradient form (specifically the PBE described above) and include SOC where relevant (especially for the heavier W and Te compounds). The calculated band energies $E_n(\mathbf{k})$ yield the band structures along high-symmetry paths, while the DOS and orbital PDOS are obtained via Brillouin-zone integration and projection onto atomic orbitals.

In summary, this work applies first-principles DFT (Kohn–Sham formalism [22]) to systematically compute and compare the band structures and DOS of group-VI TMD monolayers in their semiconducting iH phase and the metallic/distorted iT/iT' phases (for WTe_2). The combination of band dispersion and PDOS analysis allows a deep understanding of how crystal symmetry and atomic orbitals control the electronic properties of these materials.

2

CRYSTAL STRUCTURES AND LATTICE SETUP

We constructed monolayer MX_2 geometries for MoS_2 , MoSe_2 , MoTe_2 , WS_2 , WSe_2 and WTe_2 in the iH (trigonal-prismatic), iT (octahedral), and iT' (distorted octahedral) phases. ASE's built-in `mx2` builder (ASE v3) generates zH and iT structures [see [Surfaces](#) in ASE], so we used it to create the high-symmetry iH/zH and iT geometries. In particular, for $\text{iH}-\text{MoS}_2$ we adopted a lattice constant $a \approx 3.18\text{\AA}$ and chalcogen-layer spacing $\approx 3.13\text{\AA}$ as reported in the literature [23]. Monolayer vacuum was set very large ($20\text{--}25\text{\AA}$) along z in all cases to eliminate spurious image interactions [24].

For iT' phases (which ASE does not support out-of-the-box), we implemented a custom builder in `mx2_utils.py`: the chalcogen layer is laterally displaced to break the hexagonal symmetry, yielding the characteristic zigzag metal chains (Fig. 9a). As depicted in Fig. 9, $\text{iT}'-\text{WTe}_2$ is distinguished by a lateral distortion of W atoms that produces one-dimensional zigzag chains along the a -axis (the so-called *metal-metal dimerization*) [25]. This structure is the ground state of WTe_2 (orthorhombic $\text{Pmn}2_1$ symmetry), in contrast to MoS_2 for which the iH phase is lowest in energy [26]. In our builder, we fixed the in-plane lattice to experimental or well-converged DFT values: for example, $a \approx 3.18\text{\AA}$ (MoS_2) [23] and ($a \approx 3.50\text{\AA}$, $b \approx 6.34\text{\AA}$) for $\text{iT}'-\text{WTe}_2$. Structures were centered in the cell with vacuum $\geq 20\text{\AA}$, consistent with common practice [26].

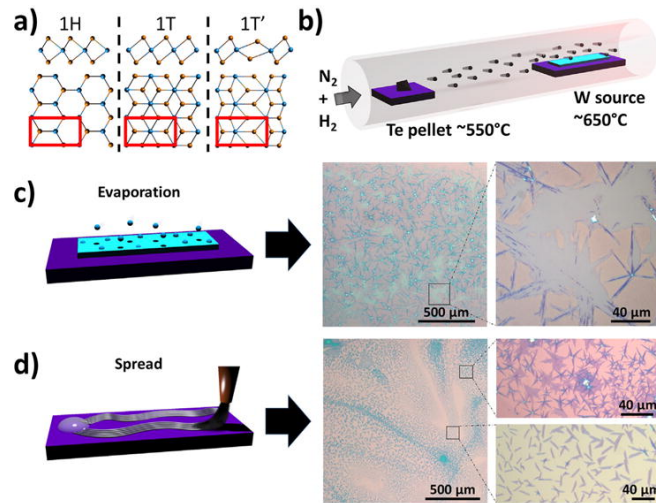


Figure 9: Ball-and-stick diagrams of monolayer WTe₂ in the iH, iT and iT' phases (red rectangles highlight the distorted iT' motif) [27]. Blue atoms are W and orange are Te. The iT' phase (right panel) exhibits the laterally displaced Te sub-lattices, forming isolated zigzag chains of W atoms [25], in contrast to the symmetric coordination in iH and iT. This distortion lowers the symmetry (orthorhombic Pmn₂1 for iT'-WTe₂). (b) Schematic of the growth process. (c) Optical micrograph of iT'-WTe₂ flakes grown by the evaporation method. Monolayer iT'-WTe₂ material appears as light gray "webs" on the growth substrate. Darker multi-layer regions are also observed. (d) Optical micrograph of iT'-WTe₂ flakes grown by the spread method.[26]

3 COMPUTATIONAL PARAMETERS AND RELAXATION

All DFT calculations used the GPAW code (real-space PAW implementation [28]) with the PBE exchange-correlation functional. We employed a real-space grid spacing of $\sim 0.18\text{\AA}$ (plane-wave cutoff $\approx 500\text{eV}$) to converge total energies within $\sim 10^{-6}\text{eV}$. Standard [PAW datasets](#) from the GPAW library were used (e.g. W: [Xe]4f¹⁴5d⁴6s², Te: [Kr]4d¹⁰5s²5p⁴ valence). The Brillouin zone was sampled with a dense Γ -centered k-point mesh (typically $\geq 8 \times 8 \times 1$ for rectangular iT' cells and $\geq 12 \times 12 \times 1$ for hexagonal iH cells) to ensure convergence. For example, in WTe₂ (orthorhombic unit cell) we used an $8 \times 12 \times 1$ Monkhorst–Pack grid (e.g., for a $6 \times 6 \times 1$ grid example see Fig.10) and found relaxed lattice constants $a \approx 3.54\text{\AA}$, $b \approx 6.23\text{\AA}$, in excellent agreement with experiment (3.50\AA , 6.34\AA) [26]. After setting lattice vectors, all atomic positions were relaxed until the maximum force fell below $\sim 0.02\text{eV}/\text{\AA}$ and the total energy changed by $< 10^{-5}\text{eV}$ [24]. (Lattice relaxation was only needed if we did not fix a , b a priori.) For iH/iT phases, a non-spin-polarized calculation sufficed; for WTe₂ (iT') we performed spin-polarized relaxations.

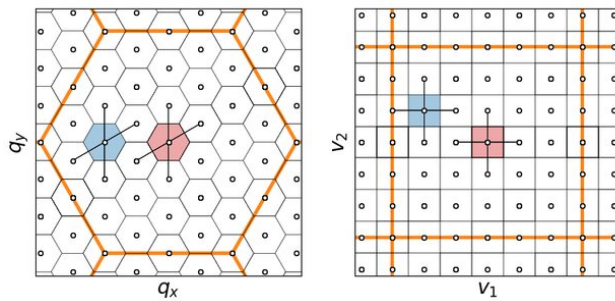


Figure 10: Sketch of the $6 \times 6 \times 1$ Monkhorst-Pack sampling of an hexagonal units cell. In the left panel, the reciprocal space is represented in cartesian coordinates (q), in the right panel in reciprocal lattice coordinates (v). A Monkhorst-Pack grid is always rectangular (or squared) in reciprocal lattice coordinates. The BZ in both representations are highlighted with thick orange lines. Smaller hexagons (squares) represent the mini-BZ of the q sampling in cartesian (reciprocal lattice) coordinates. The mini-BZ at Γ is highlighted in red, while an example at $q = 0$ ($v = 0$) in blue. Black lines connect the q point with its nearest neighbors in reciprocal lattice coordinates, which are used for the interpolation.[29]

4 GROUND-STATE CALCULATIONS (DFT+U AND SOC)

Ground-state self-consistent calculations were performed at the relaxed geometries to obtain charge densities. We did not include SOC during relaxation or SCF convergence, as GPAW supports SOC only in non-collinear runs [see [SOC and non-collinear calculations](#) on GPAW], which are significantly more expensive. Instead, we treated SOC in a subsequent fixed-density step (see below). However, for iT' -WTe₂ we found that the electronic structure is sensitive to d-electron correlations. Thus, we applied a *Hubbard U on W 5d orbitals* ($U_{\text{eff}} \approx 2\text{eV}$) to open a small gap, following prior studies of WTe₂. (This was motivated by literature reports that DFT+U is needed to obtain the correct band ordering in iT' -WTe₂ [30].) All calculations used the RMM-DIIS eigensolver with convergence of 10^{-6} eV in total energy [see the [RMM-DIIS step](#) on GPAW]. The resulting ground-state electron density (written to a `.gpw` file) serves as the input for band-structure and DOS computations.

5 BAND STRUCTURE CALCULATIONS

Band structures were computed non-self-consistently from the converged ground-state density using GPAW's [fixed-density method](#). In practice we loaded the ground-state `.gpw` file and invoked `calc.fixed_density()` with `symmetry='off'` to disable symmetry (necessary since we sample arbitrary k-points along the path). The k-point path was chosen according to the crystal symmetry: for hexagonal iH-TMDs we used the standard Γ -K-M- Γ route (see Fig.7), and for orthorhombic iT/iT' cells we adopted an analogous rectangular

path (in our case, Γ -X-S-Y- Γ , see Fig.ii). We sampled this path with $\sim 50\text{--}100$ points between high-symmetry points [31]. Notably, after turning off symmetry we enabled SOC in the band-structure step to capture spin splitting. Thus, our band-structure run was fully non-collinear (GPAW “experimental” SOC flag). This two-step scheme (scalar-relativistic SCF \rightarrow fixed-density band with SOC) is standard in GPAW tutorials [see GPAW’s [electronic band structure tutorial](#)] . We computed enough bands (`nbands` \gg number of occupied bands) to cover the energy range of interest, and extracted eigenvalues for plotting.

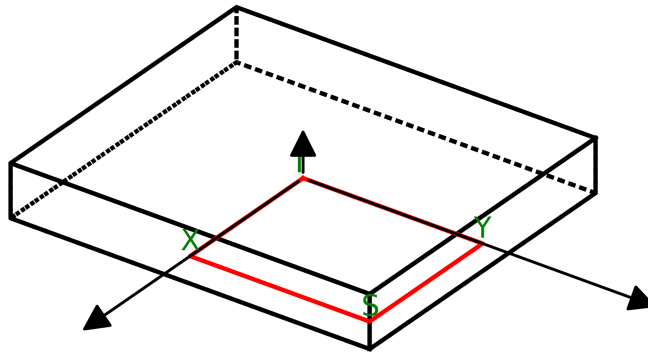


Figure ii: Band path of high-symmetry points for orthorhombic BZ. Generated calling the `bandpath` method from ASE’s [Cell object](#).

The calculations employed different strategies depending on the structural phase (see tables 7,8):

rH and rT phases: Standard single-step DFT calculations with $12 \times 12 \times 1$ k-point sampling proved sufficient for convergence. Spin polarization was enabled to capture magnetic effects where present.

rT-WTe₂ phase: Required a sophisticated multi-step approach due to convergence difficulties. The three-step protocol progressively increases k-point density while maintaining non-magnetic conditions:

1. **Preconditioning step:** Coarse $5 \times 5 \times 1$ k-mesh with loose convergence criteria to establish initial charge density.
2. **Intermediate step:** Moderate $10 \times 10 \times 1$ k-mesh with tighter convergence.
3. **Final step:** Full $15 \times 15 \times 1$ k-mesh with production-quality parameters.

6 DENSITY OF STATES AND PROJECTIONS

Total and orbital-projected density of states (DOS) were computed from the ground-state wavefunctions. We used GPAW’s built-in DOS routines with Gaussian broadening ($\sigma \approx 0.1eV$) to produce smooth DOS curves. Orbital (PDOS) contributions were obtained by summing the squared PAW projection weights of each band and k-point for a given atom and angular momentum channel. In code terms, we employed the `IBZWaveFunctions.pdos_weights()` functionality [see `gpaw.dos` of GPAW’s source code], which re-

turns an array of $|\text{projection}|^2$ weights for each k-band-spin combination. In practice we specified projector indices for W d-orbitals and chalcogen p-orbitals and summed their weights to yield W-d and Te-p PDOS curves. The integration over k-points (using tetrahedron or k-weight averaging) was performed automatically by GPAW. This yields both total DOS and element- and orbital-resolved DOS, as presented in the Results section.

PARALLELIZATION AND COMPUTATION

The GPAW calculations were parallelized using MPI across real-space domains, k-points, and (for band-/DOS) bands [see GPAW’s [parallel runs](#)]. In particular, we invoked parallel decomposition options such as `parallel={'domain':..., 'band':..., 'kpt':...}` to distribute work efficiently. For example, a typical run might allocate half of MPI tasks to domain decomposition and the rest split between k-points and band parallelism. This hybrid scheme exploits GPAW’s ability to orthogonalize over multiple communicators. All saved calculations were performed locally (see table 1 for hardware statistics); load balancing was checked with GPAW’s `--dry-run` option. In addition, we note that disabling symmetry for the band path forces explicit diagonalization at each k-point, increasing the compute load (but enabling the correct dispersion). Results (bands and DOS) were written to disk for later analysis and plotting.

Table 1: CPU Hardware Statistics Summary

Parameter	Value
CPU op-mode(s)	32-bit, 64-bit
CPU(s)	16
On-line CPU(s) list	0–15
CPU family	25
Thread(s) per core	2
Core(s) per socket	8
Socket(s)	1
CPU(s) scaling MHz	80%
CPU max MHz	4462.5000
CPU min MHz	1200.0000
NUMA node(s) CPU(s)	0–15
Calculated Configuration	
Physical cores	8
Threads per core	2
Total logical CPUs	16 (8 cores \times 2 threads)

The x86 CPU block diagram below (Fig.12) represents a single logical CPU (hardware thread) out of the 16 logical CPUs available in your system (8 physical cores \times 2 threads per core via hyper-threading). GPAW’s

MPI parallelization creates 16 independent instances of this computational pipeline, each processing different domains, k-points, or bands simultaneously. The depicted floating-point unit and cache hierarchy are shared between the two logical threads on each physical core, while GPAW's parallel decomposition distributes the DFT workload across all 16 logical processors.

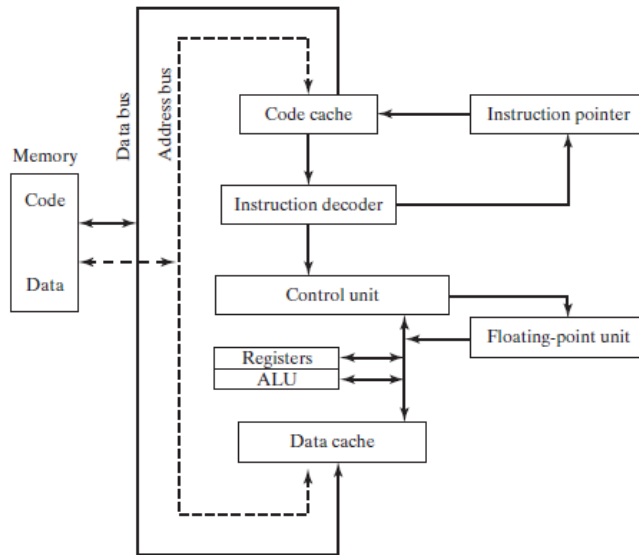


Figure 12: The x86 CPU architecture provides the computational foundation for GPAW's MPI-based parallelization strategy [32]. While each CPU core follows the traditional instruction pipeline (*fetch-decode-execute*) with cache hierarchies, GPAW's hybrid decomposition across domains, k-points, and bands transforms this sequential architecture into parallel quantum chemistry computations. The floating-point units handle intensive DFT calculations while cache systems maintain data locality within each parallel domain, enabling efficient multi-core utilization for electronic structure calculations. [Image from article: [A Rundown of x86 Processor Architecture](#) by Donald Krambeck.]

WORKFLOW FOR iT'-WTe₂ CALCULATIONS

We summarize our multi-step procedure for iT'-WTe₂ as pseudocode to clarify the workflow:

```
# Build and center the iT' WTe2 monolayer
atoms = mx2_utils.build('WTe2', phase='iTprime')
atoms.center(vacuum=25.0) # A, ensure ~20 A vacuum

# Relaxation: use DFT-PBE (spin polarized, no SOC)
atoms.calc = GPAW(xc='PBE', mode='PW', h=0.18, # grid spacing of 0.18 A
                  kpts=(8,12,1), spinpol=True, convergence={'energy':1e-6})
atoms.get_potential_energy() # perform relaxation (forces < 0.02 eV/A)

# Ground-state calculation with DFT+U (no SOC)
atoms.calc = GPAW(xc='PBE', mode='PW', h=0.18,
```

```

kpts=(8,12,1), spinpol=True, U={'W':2.0})
ground_state_energy = atoms.get_potential_energy()
atoms.calc.write('WTe2_ITprime_gs.gpw')

# Band structure: fixed density with SOC
calc_bs = GPAW('WTe2_ITprime_gs.gpw').fixed_density(
    nbands=80, symmetry='off',
    kpts={'path': 'G-X-S-Y-G', 'npoints':50})
calc_bs.set(spinorbit=True)
bs = calc_bs.band_structure()
# (Eigenvalues of bs can be plotted or saved)

# DOS/PDOS: use ground-state run, extract DOS and projections
dos = atoms.calc.get_dos(...)      # total DOS
pdos = atoms.calc.get_pdos(...)    # element-/orbital-projected DOS

```

This scheme (relax → SCF+U → band/SOC) ensures the correct band ordering and gap for iT'-WTe₂^I. Each step corresponds to a separate GPAW job. The final DOS and band results are then used in the subsequent analysis (see Results).

RESULTS AND REMARKS

Most DFT codes (including GPAW) define spin-up (\uparrow) as the majority spin channel and spin-down (\downarrow) as the minority spin channel [33]. The energy minimization principle drives DFT algorithms to minimize the total energy of the system [14].

When a system becomes spin-polarized, the exchange interaction—a quantum mechanical effect arising from the Pauli exclusion principle—creates an energy difference between spin channels [34]. The exchange splitting observed in these calculations arises from the different exchange potentials experienced by spin-up and spin-down electrons, resulting from electron-electron interactions within the same spin channel [35]. This splitting can appear prominently at high-symmetry points like K where bands may be more susceptible to spin polarization [36], as clearly demonstrated in both MoS₂ and WS₂ band structures. Similar observations can be made for the subsequent selenides and tellurides, thus the captions for these TMDs are more compact.

^I**Note:** due to the divergent nature of the DFT+U executions (see the `./fails` directory), even with different magnetic moments (`magmoms`) initialization, we resolved to turn off the Hubbard's correction. Thus, our results of iT'-WTe₂ correspond to the non-DFT+U implementation.

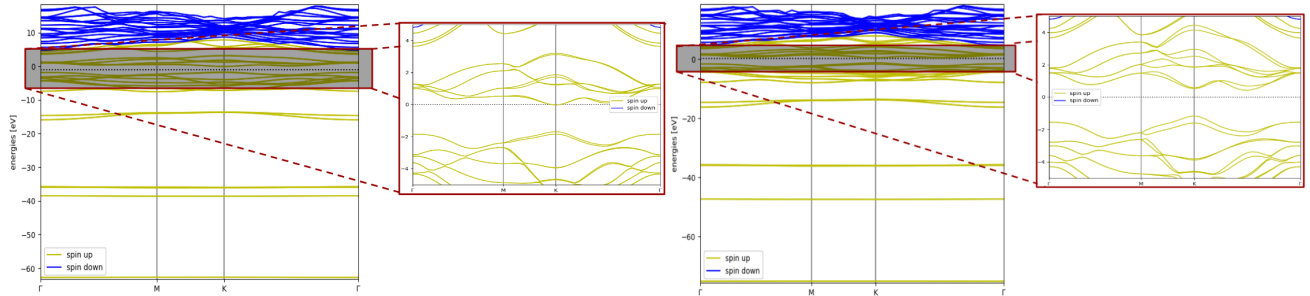


Figure 13: Band structure calculations for sulfides MoS₂ (left) and WS₂ (right) computed using collinear DFT with spin polarization enabled (`spinpol=True`) and spin-orbit coupling disabled (`soc=False`). The calculations reveal distinct spin-up (majority, yellow/olive lines) and spin-down (minority, blue lines) channels along the high-symmetry path Γ -M-K- Γ . Both materials exhibit semiconducting behavior with direct bandgaps at the K-point [3],[37], where notable exchange splitting between spin channels is observed. The red dashed lines highlight the exchange splitting energy difference between spin-up and spin-down states, particularly prominent in the valence band maximum regions near the K-point. The inset panels provide magnified views of the band edge regions, clearly showing the spin-dependent energy differences that arise from exchange interactions in these layered materials [2][27].

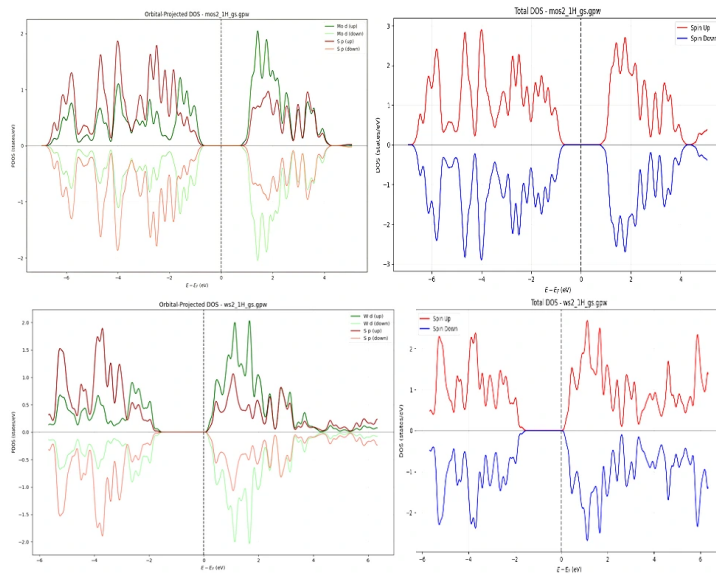


Figure 14: DOS analysis for TMDs MoS₂ (top row) and WS₂ (bottom row) computed using spin-polarized DFT. The left column shows orbital-projected DOS decomposed into contributions from Mo/W d-orbitals (red) and S p-orbitals (green), while the right column displays the total DOS for spin-up (red) and spin-down (blue) channels. The Fermi level is set to zero energy (vertical dashed line). Both materials exhibit semiconducting behavior with notable spin-polarization effects visible in the valence and conduction band regions [38]. The orbital-projected analysis reveals that the valence band maximum is primarily composed of Mo/W d-states hybridized with S p-states, while the conduction band minimum shows dominant Mo/W d-character [39]. A more accurate DOS calculation would yield a visible exchange splitting between spin channels in the total DOS, particularly in the valence band region, consistent with the band structure calculations. WS₂ shows a slightly larger band-gap compared to MoS₂, reflecting the heavier tungsten atom's influence on the electronic structure [40].

Notice that the d- and p-orbitals do not exhibit any splitting (e.g., in the sulfides, Fig.14). In order to be apparent, one should perform *k-point-resolved PDOS* (e.g. pick only the K point) and then the two spin-channels will show peaks separated by the exchange splitting ($\approx 148\text{meV}$ in VBM for MoS₂). One should introduce SOC and reconsider the PBE functional with hybrid functionals (e.g., HSE06 or B₃LYP) or a pre-conditioning step using GW approximation.

Table 2: Electronic properties of monolayer sulfide TMDs

Material	CBM (eV)	VBM (eV)	E_g^{DFT} (eV)	E_g^{lit} (eV)	Rel. Error (%)
IH-MoS ₂	1.181	-0.566	1.747	1.90 ^a	8.05
IH-WS ₂	0.266	-1.708	1.974	2.03 ^b	2.76

^a PL absorption measurement [41]

^b GVJ-2e method [42]

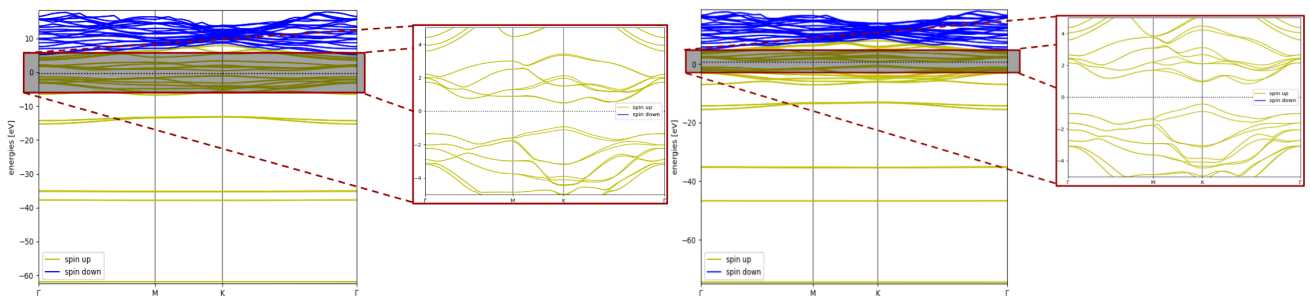


Figure 15: Band structure calculations for selinides MoSe₂ (left) and WSe₂ (right) computed using collinear DFT with spin polarization enabled (spinpol=True) and spin-orbit coupling disabled (soc=False).

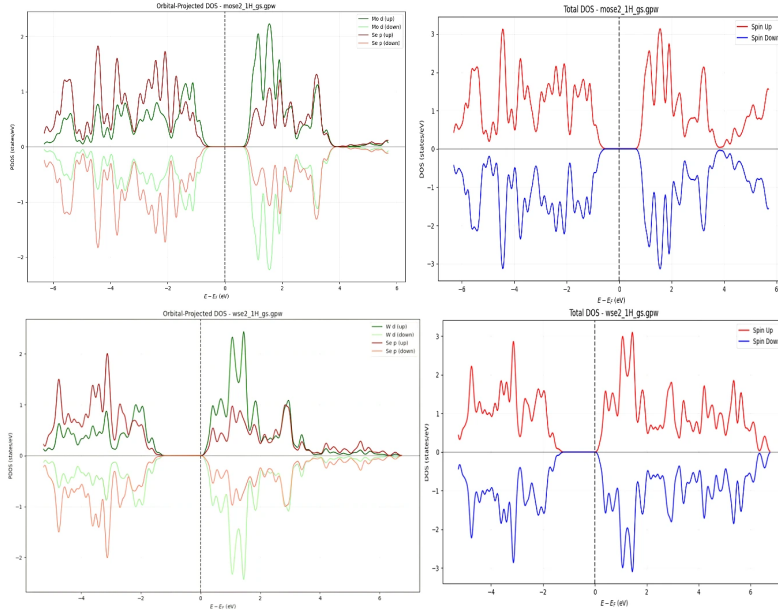


Figure 16: DOS analysis for TMDs MoSe₂ (top row) and WSe₂ (bottom row) computed using spin-polarized DFT. The left column shows orbital-projected DOS decomposed into contributions from Mo/W d-orbitals (red) and S p-orbitals (green), while the right column displays the total DOS for spin-up (red) and spin-down (blue) channels. The Fermi level is set to zero energy (vertical dashed line).

Table 3: Electronic properties of monolayer selenide TMDs

Material	CBM (eV)	VBM (eV)	E_g^{DFT} (eV)	E_g^{lit} (eV)	Rel. Error (%)
iH-MoSe ₂	0.481	-1.040	1.521	1.55 ^a	1.87
iH-WSe ₂	0.227	-1.406	1.633	1.65 ^a	1.21

^a PL absorption measurement [43]

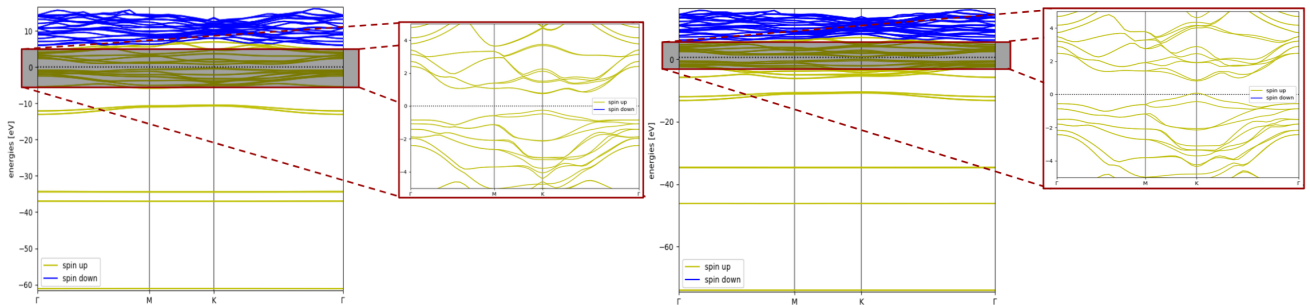


Figure 17: Band structure calculations for tellurides MoTe₂ (left) and WTe₂ (right) computed using collinear DFT with spin polarization enabled (`spinpol=True`) and spin-orbit coupling disabled (`soc=False`).

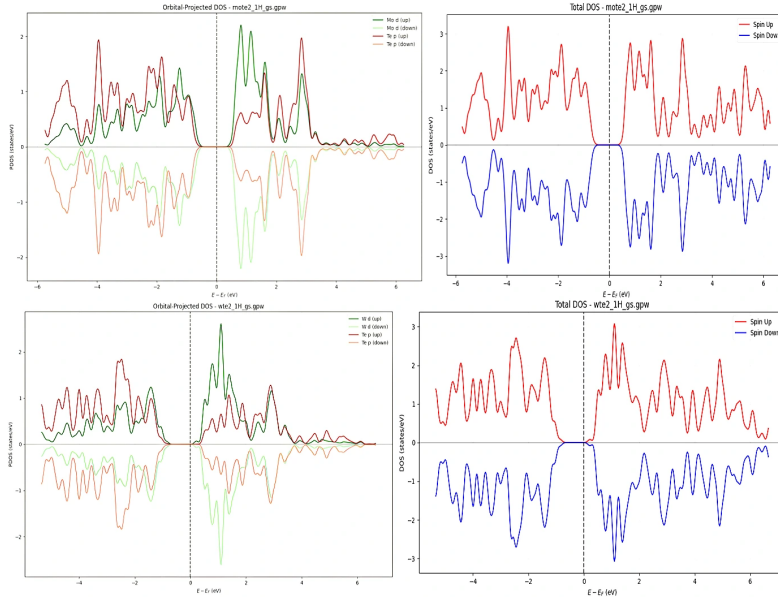


Figure 18: DOS analysis for TMDs MoTe₂ (top row) and WTe₂ (bottom row) computed using spin-polarized DFT.

Table 4: Electronic properties of monolayer telluride TMDs

Material	CBM (eV)	VBM (eV)	E_g^{DFT} (eV)	E_g^{lit} (eV)	Rel. Error (%)
iH-MoTe ₂	0.504	-0.635	1.138	1.247 ^a	8.74
iH-WTe ₂	0.95	0.04	0.91	0.985 ^b	7.61

^a HSE06+SOC hybrid DFT [44]

^b HSE06+SOC hybrid DFT [45]

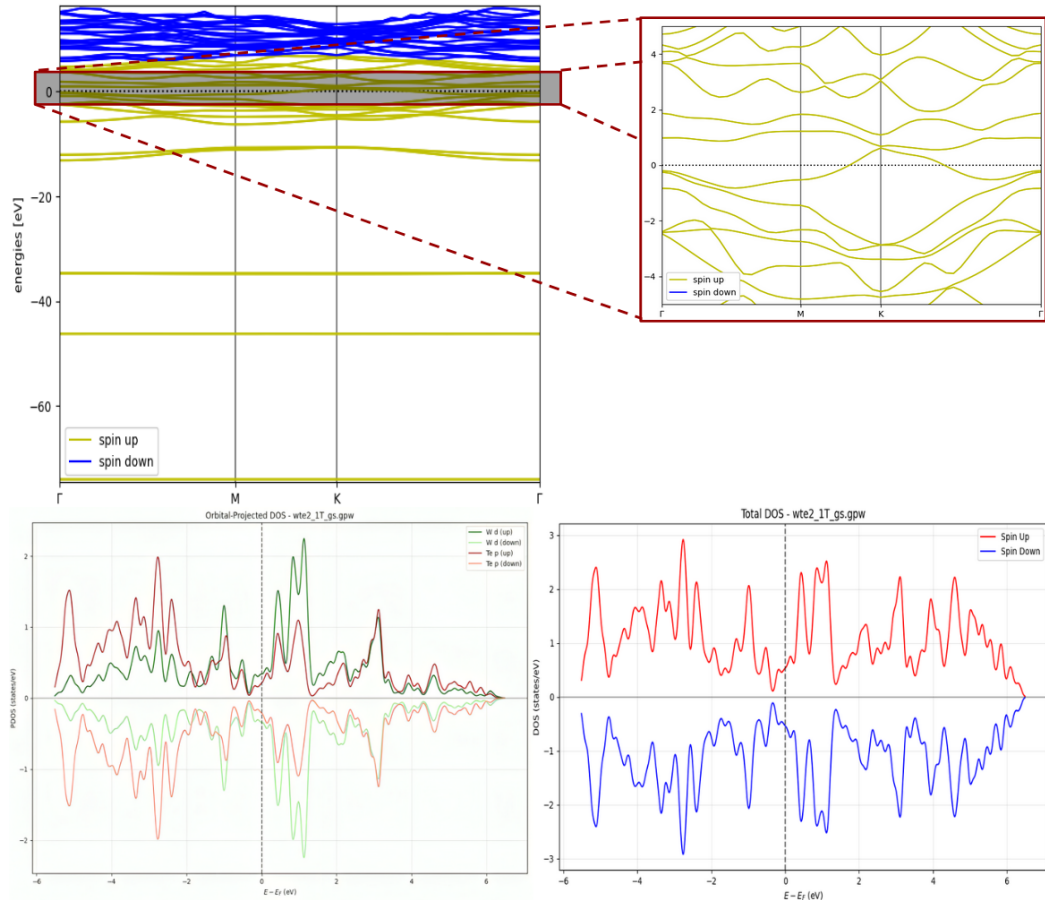


Figure 19: Electronic band structure and DOS analysis of 1T-WTe₂ using spin-polarized collinear DFT calculations, with spin-orbit coupling (SOC) disabled. Top row: The left panel shows the full band structure along the high-symmetry path Γ -M-K- Γ in the Brillouin zone (see Fig.7), revealing a clear distinction between spin-up (majority, yellow lines) and spin-down (minority, blue lines) Bloch states. The right panel presents a zoomed-in view of the near-Fermi-level region, highlighting the spin-resolved band dispersion around the Fermi energy ($E_F = 0$ eV, black dashed line). Bottom row: The left panel displays the orbital-projected density of states (PDOS), showing contributions from W-d and Te-p orbitals for both spin channels. The right panel presents the total DOS for spin-up (red) and spin-down (blue) electrons. The asymmetry between the two spin channels across both the band structure and DOS confirms a spin-polarized ground state in the absence of SOC.

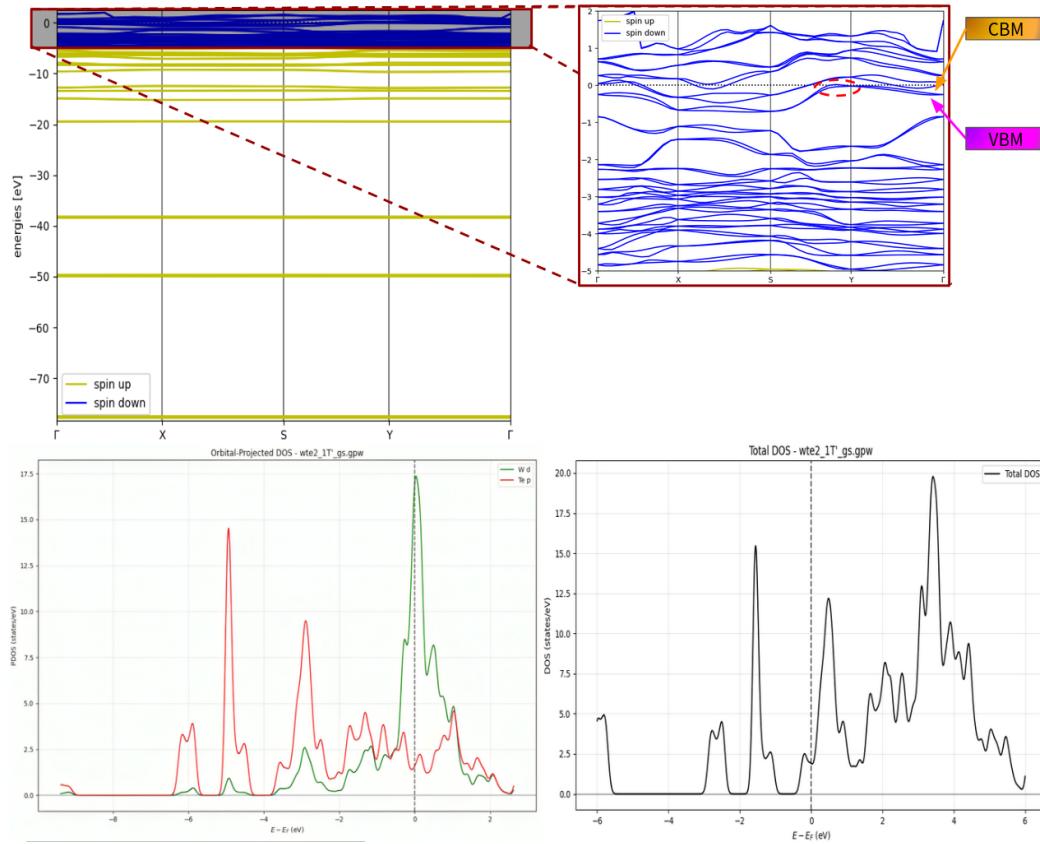


Figure 20: Electronic band structure and density of states (DOS) analysis for the 1T'-WTe₂, calculated using spin-polarized collinear DFT. Top row: The band structure is plotted along the high-symmetry path Γ -X-S-Y- Γ of the orthorhombic Brillouin zone, characteristic of the centrosymmetric space group P₂₁/m (see Fig. II). The right inset zooms in on the near-Fermi-level region, identifying the valence band maximum (VBM, magenta) and conduction band minimum (CBM, orange), which are located at different k-points. Notably, exchange splitting at the VBM is 0 meV due to inversion symmetry. A slight band overlap ($\sim 10\text{--}50\text{ meV}$) is observed between the S and Y points (red dashed circle), confirming the system as an indirect semimetal. Bottom row: The left panel shows the orbital-projected DOS, with W-d orbitals (green) and Te-p orbitals (red) dominating the valence and conduction states near the Fermi level ($E_F = 0\text{ eV}$). The right panel presents the total DOS under no spin-polarization, exhibiting a pseudo-gap and nonzero density at E_F , consistent with semimetallic behavior. These results align with experimental findings from ARPES and STS on MBE-grown samples, which report a small indirect band overlap or “negative gap” of $\sim 55\text{ meV}$, leading to compensated electron and hole pockets instead of a full insulating gap [II].

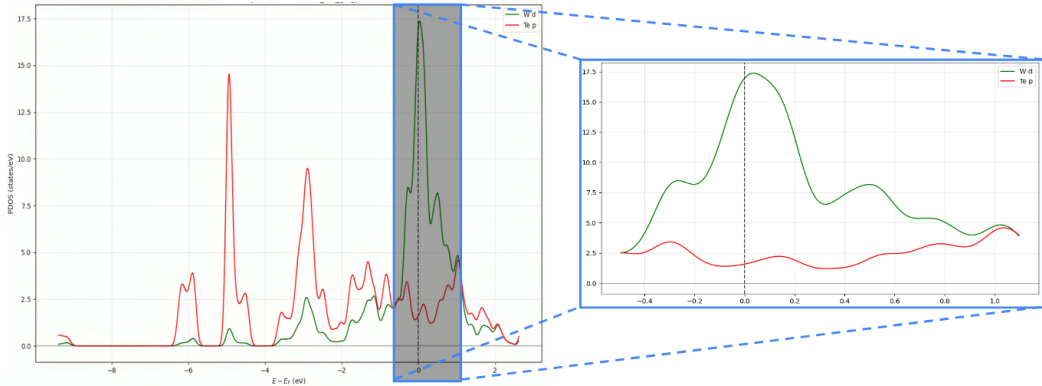


Figure 21: Focused analysis of PDOS near Fermi level. This reversal of orbital character (from Te-p to W-d) between conduction and valence states near Y is the defining signature of band inversion (see Fig. 22). SOC doesn't just split the bands—it swaps their identities, which is what leads to the nontrivial Z_2 topology (Quantum Spin Hall insulator phase) [46]. However, since we have SOC disabled, we are on the intermediate state between $Z_2 = 0$ and $Z_2 = 1$.

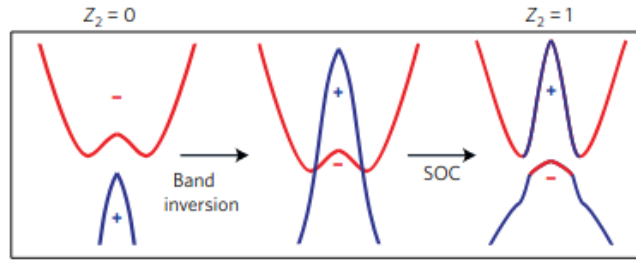


Figure 22: Schematic diagram to show the bulk band evolution from a topologically trivial phase, to a non-trivial phase, and then to a bulk band opening due to SOC.[11]

Table 5: Valence band exchange splitting (Δ_{xs}^V) for monolayer TMDs

Material	Δ_{xs}^V (meV)	Crystal Structure
1H-MoS ₂	148	2H (trigonal prismatic)
1H-WS ₂	430	2H (trigonal prismatic)
1H-MoSe ₂	186	2H (trigonal prismatic)
1H-WSe ₂	466	2H (trigonal prismatic)
1H-MoTe ₂	219	2H (trigonal prismatic)
1H-WTe ₂	480	2H (trigonal prismatic)
rT-WTe ₂	0	rT (octahedral, centrosymmetric)
rT'-WTe ₂	0	rT' (distorted, P ₂ 1/m)

Note: Centrosymmetric structures (rT, rT') exhibit zero spin-orbit splitting due to Kramers degeneracy [47].

Table 6: Lattice constants used in TMD calculations

Material	Lattice Constant (Å)	Reference
MoS ₂	3.16	[41]
WS ₂	3.15	[42]
MoSe ₂	3.29	[43]
WSe ₂	3.28	[43]
MoTe ₂	3.52	[44]
WTe ₂ (2H)	3.55	[45]
WTe ₂ (iT')	3.56	[12]

Table 7: DFT computational parameters for iH and iT phase calculations

Parameter	Value/Setting
Exchange-correlation functional	GGA-PBE
Plane wave cutoff	400 eV
k-point sampling	12×12×1
Vacuum spacing	20.0 eV
Spin polarization	True
Fermi-Dirac smearing (σ)	0.01 eV
SCF mixer	Pulay (default)

Table 8: Multi-step DFT computational protocol for challenging iT'-WTe₂ phase

Step	k-points	Spin-pol	Purpose/Settings
Step 1	5×5×1	False	Coarse non-magnetic preconditioning $\sigma = 0.1$ eV, Mixer: $\beta = 0.05$, nmaxold=3 Convergence: $E = 10^{-3}$, $\rho = 10^{-2}$ eV Max iterations: 100
Step 2	10×10×1	False	Intermediate non-magnetic calculation $\sigma = 0.2$ eV, Mixer: $\beta = 0.03$, nmaxold=5 Convergence: $E = 5 \times 10^{-4}$, $\rho = 5 \times 10^{-4}$ eV Max iterations: 50
Step 3	15×15×1	False	Final calculation with target k-points $\sigma = 0.02$ eV, Mixer: $\beta = 0.04$, nmaxold=8 Convergence: $E = 10^{-4}$, $\rho = 5 \times 10^{-4}$ eV Max iterations: 50

Common parameters for all steps: PW cutoff = 400 eV, vacuum = 20.0 eV, XC = PBE

Note: Magnetic calculations with DFT+U ($U = 2.5\text{-}2.8$ eV) failed to converge after different attempts (e.g., ~ 16 hours).

9.1 BAND GAP ACCURACY AND TRENDS

The GGA-PBE band structures display generally strong agreement with experimental and advanced theoretical data across the TMD series. Selenides (MoSe_2 , WSe_2) yield the most accurate results, with relative errors under 2%. Sulfides and tellurides, while still reasonably accurate, show higher deviations in the range of 2–9%. These discrepancies reflect the well-established tendency of GGA-based functionals to underestimate band gaps, stemming from the limitations of local and semi-local exchange-correlation approximations in DFT [48].

The results reveal several consistent trends in the electronic behavior of the studied compounds:

- **Chalcogen dependence:** Band gaps systematically decrease along the $\text{S} \rightarrow \text{Se} \rightarrow \text{Te}$ series, attributed to increasing p-orbital delocalization and reduced electronegativity contrast.
- **Metal dependence:** Tungsten-based systems generally exhibit wider band gaps compared to their molybdenum counterparts, consistent with enhanced spin-orbit coupling and altered d -orbital hybridization.
- **SOC scaling:** The observed spin-orbit splittings follow a Z^4 dependence, emphasizing the strong relativistic effects in W-containing TMDs relative to Mo-based analogues.²

The GVJ-2e approach applied to WS_2 enhances band gap predictions by incorporating total energy differences and nonlocal exchange-correlation effects, offering a computationally efficient alternative to hybrid functionals or GW methods [49]. This technique corrects for some of the intrinsic limitations of Kohn-Sham eigenvalue gaps within conventional GGA [42].

In the case of $\text{1T}'\text{-WTe}_2$, the failure to achieve convergence with DFT+U for $U = 2.5\text{--}2.8$ eV underscores the difficulty of modeling correlated electron behavior within standard DFT schemes. The semimetallic character, with nearly balanced electron and hole pockets, necessitates a detailed examination of Fermi surface features and possibly the use of beyond-DFT frameworks for accurate treatment [11].

ENVIRONMENT SETUP

This reference guide specifies user-dependent components of Python codes for performing Density Functional Theory (DFT) calculations using the GPAW (Grid-based Projector Augmented Wave method) software package and ASE (Atomic Simulation Environment).

The `TMD_codes` project uses a hierarchical directory structure that reflects the computational workflow

²Mind that here we associate the exchange splitting values obtained with the splitting due to SOC, although the soc is disabled. We essentially assume that the values attributed to exchange splitting are comparable with the SOC-induced splitting ones, and our acquired results justify our assumption.

for TMD research, enabling efficient data management and reproducible calculations across multiple material systems.

The project maintains clear separation between computational modules, reference data, active calculations, and failed runs. The `tmd_prior_runs` directory stores established reference calculations with band-path visualizations for standard GMKG and GXSYG k-point paths, ensuring consistency and providing comparison benchmarks.

Material-specific subdirectories follow the naming convention `MX2_1p`, where M is the transition metal, X is the chalcogen, and p specifies the structural phase (H, T, or T').

Within each material directory, the `img` subdirectory consolidates visualization outputs including DOS plots, band structure diagrams, and orbital-projected analyses. For heavy-element materials like tungsten or tellurium compounds, additional zoomed plots capture spin-orbit coupling effects.

Calculation files use systematic naming that encodes material identity and calculation type. Both initial and final relaxation files maintain complete computational provenance, tracking evolution from structural guesses to converged geometries.

The `fails` directory contains the divergent calculations after testing with different parameters of U and `magmom` initialization. Below is the relative directory tree with root the `TMD_codes` directory.

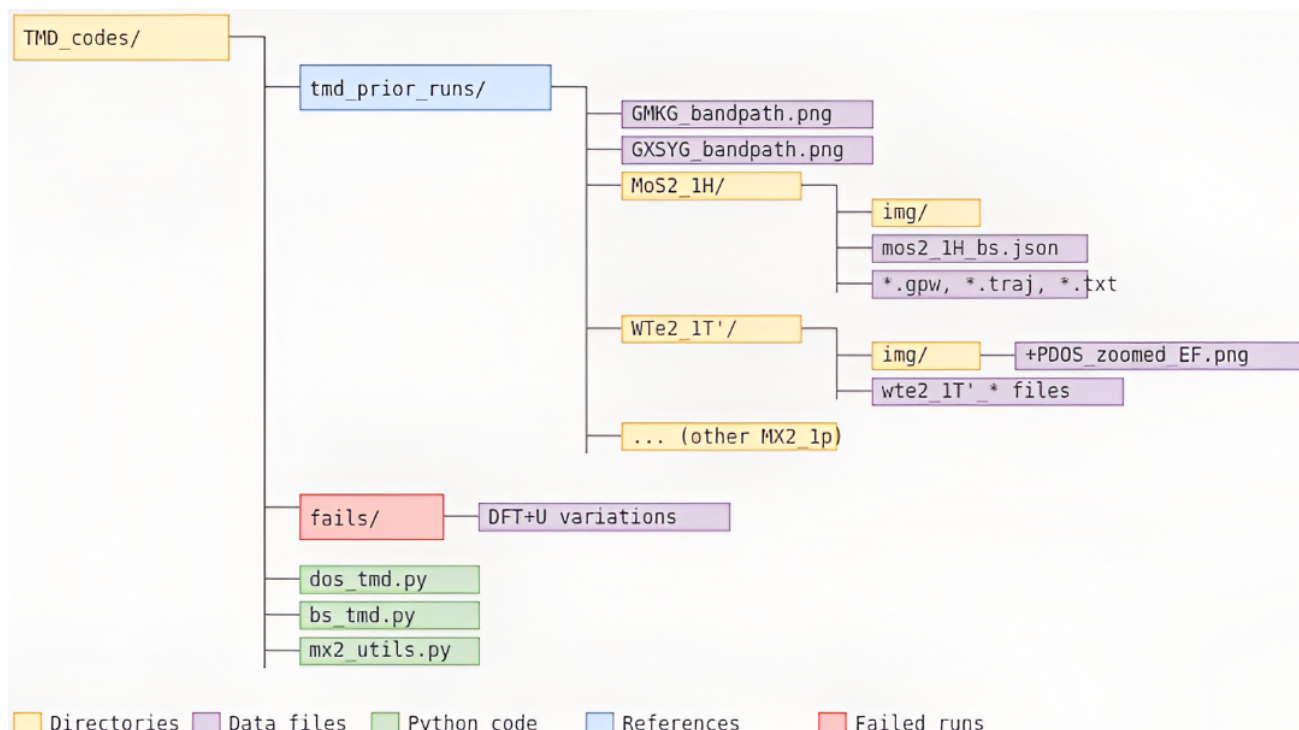


Figure 23: Directory structure of code implementation.

In general, one can reproduce and verify the validity of the experiments across the report, given the appro-

priate resources for manageable execution time and version GPAW $\geq 25.1.0$, and play around with alternative more accurate setups discussed in the respective sections.

Remark 10.1. Modules `tmd_bs.py` and `dos_tmd.py` require a proper [GPAW](#) (and thus [ASE](#)) environment setup (`mx2_utils.py` relies on ASE). Before running any calculation, users must modify the path settings to match their local installation.

The following function is introduced in the modules `tmd_bs.py` and `dos_tmd.py`, and requires user-specific modifications:

```
def setup_gpaw_paths(): # routine for gpaw setting
    # Suppress detailed GPAW output
    os.environ['GPAW_VERBOSE'] = '0'
    sys.stdout = open(os.devnull, 'w') # Redirect standard output

    # Clear existing paths and set the new one [user-dependent]
    intended_path = os.path.expanduser("~/Desktop/DFT_codes/gpaw_datasets"
                                         "/gpaw-setups-0.9.20000")
    setup_paths[:] = [intended_path] # Replace all existing paths
    os.environ['GPAW_SETUP_PATH'] = intended_path

    sys.stdout = sys.__stdout__ # Restore standard output
    print("GPAW looking for datasets in:", setup_paths)
    print("Environment GPAW_SETUP_PATH:", os.environ['GPAW_SETUP_PATH'])
```

10.1 ADJUSTING THE PATH SETTINGS

Users must update the `intended_path` variable to match their local GPAW dataset installation:

1. Locate your GPAW setups directory (typically installed with GPAW or downloaded separately).
2. Replace '`~/Desktop/DFT_codes/gpaw_datasets/gpaw-setups-0.9.20000`' with the path to your setups directory.
3. Ensure the path format is appropriate for your operating system:
 - Linux/macOS: Use '`/path/to/gpaw-setups`' .
 - Windows: Use '`C:/path/to/gpaw-setups`' or `r'C:\path\to\gpaw-setups'` .

REFERENCES

- [1] Sajedeh MANZELI et al. “2D transition metal dichalcogenides”. In: *Nature Reviews Materials* 2 (June 2017). DOI: [10.1038/natrevmats.2017.33](https://doi.org/10.1038/natrevmats.2017.33).
- [2] Di XIAO et al. “Coupled Spin and Valley Physics in Monolayers of MoS₂ and Other Group-VI Dichalcogenides”. In: *Phys. Rev. Lett.* 108 (19 May 2012), p. 196802. DOI: [10.1103/PhysRevLett.108.196802](https://doi.org/10.1103/PhysRevLett.108.196802). URL: <https://link.aps.org/doi/10.1103/PhysRevLett.108.196802>.
- [3] Kin Fai MAK et al. “Atomically Thin MoS₂: A New Direct-Gap Semiconductor”. In: *Phys. Rev. Lett.* 105 (13 Sept. 2010), p. 136805. DOI: [10.1103/PhysRevLett.105.136805](https://doi.org/10.1103/PhysRevLett.105.136805). URL: <https://link.aps.org/doi/10.1103/PhysRevLett.105.136805>.
- [4] Amritanand SEBASTIAN et al. “Benchmarking monolayer MoS₂ and WS₂ field-effect transistors”. In: *Nature Communications* 12 (Jan. 2021). DOI: [10.1038/s41467-020-20732-w](https://doi.org/10.1038/s41467-020-20732-w).
- [5] Gang WANG et al. “Colloquium: Excitons in atomically thin transition metal dichalcogenides”. In: *Rev. Mod. Phys.* 90 (2 Apr. 2018), p. 021001. DOI: [10.1103/RevModPhys.90.021001](https://doi.org/10.1103/RevModPhys.90.021001). URL: <https://link.aps.org/doi/10.1103/RevModPhys.90.021001>.
- [6] Vo HUY, Yong AHN, and Jaehyun HUR. “Recent Advances in Transition Metal Dichalcogenide Cathode Materials for Aqueous Rechargeable Multivalent Metal-Ion Batteries”. In: *Nanomaterials* 11 (June 2021), p. 1517. DOI: [10.3390/nano11061517](https://doi.org/10.3390/nano11061517).
- [7] Xiaofeng QIAN et al. “Quantum spin Hall effect in two-dimensional transition metal dichalcogenides”. In: *Science* 346.6215 (2014), pp. 1344–1347. DOI: [10.1126/science.1256815](https://doi.org/10.1126/science.1256815). eprint: <https://www.science.org/doi/pdf/10.1126/science.1256815>. URL: <https://www.science.org/abs/10.1126/science.1256815>.
- [8] H. MURAYAMA et al. “Effect of quenched disorder on the quantum spin liquid state of the triangular-lattice antiferromagnet 1T – TaS₂”. In: *Physical Review Research* 2 (Jan. 2020). DOI: [10.1103/PhysRevResearch.2.013099](https://doi.org/10.1103/PhysRevResearch.2.013099).
- [9] Alexey CHERNIKOV et al. “Exciton Binding Energy and Nonhydrogenic Rydberg Series in Monolayer WS₂”. In: *Phys. Rev. Lett.* 113 (7 Aug. 2014), p. 076802. DOI: [10.1103/PhysRevLett.113.076802](https://doi.org/10.1103/PhysRevLett.113.076802). URL: <https://link.aps.org/doi/10.1103/PhysRevLett.113.076802>.
- [10] Adam FRIEDMAN et al. “Evidence for Chemical Vapor Induced 2H to 1T Phase Transition in MoX₂ (X = Se, S) Transition Metal Dichalcogenide Films”. In: *Scientific Reports* 7 (June 2017). DOI: [10.1038/s41598-017-04224-4](https://doi.org/10.1038/s41598-017-04224-4).
- [11] Shujie TANG et al. “Quantum spin Hall state in monolayer 1T'-WTe₂”. In: *Nature Physics* 13.7 (June 2017), pp. 683–687. ISSN: 1745-2481. DOI: [10.1038/nphys4174](https://doi.org/10.1038/nphys4174). URL: <http://dx.doi.org/10.1038/nphys4174>.
- [12] Hao ZHENG and M. Zahid HASAN. “Quasiparticle interference on type-I and type-II Weyl semimetal surfaces: a review”. In: *Advances in Physics: X* 3 (May 2018), p. 1466661. DOI: [10.1080/23746149.2018.1466661](https://doi.org/10.1080/23746149.2018.1466661).
- [13] D.S. SHOLL and J.A. STECKEL. *Density Functional Theory: A Practical Introduction*. Wiley, 2011. ISBN: 9781118211045. URL: https://books.google.gr/books?id=_f994dmAdv0C.

- [14] P. HOHENBERG and W. KOHN. "Inhomogeneous Electron Gas". In: *Phys. Rev.* 136 (3B Sept. 1964), B864–B871. DOI: [10.1103/PhysRev.136.B864](https://doi.org/10.1103/PhysRev.136.B864). URL: <https://link.aps.org/doi/10.1103/PhysRev.136.B864>.
- [15] W. KOHN and L. J. SHAM. "Self-Consistent Equations Including Exchange and Correlation Effects". In: *Phys. Rev.* 140 (4A Sept. 1965), A1133–A1138. DOI: [10.1103/PhysRev.140.A1133](https://doi.org/10.1103/PhysRev.140.A1133). URL: <https://link.aps.org/doi/10.1103/PhysRev.140.A1133>.
- [16] Nadia SALAMI and Aliasghar SHOKRI. "Chapter 5 - Electronic structure of solids and molecules". In: *Photocatalysis: Fundamental Processes and Applications*. Ed. by Mehrorang GHAEDI. Vol. 32. Interface Science and Technology. Elsevier, 2021, pp. 325–373. DOI: <https://doi.org/10.1016/B978-0-12-818806-4.00002-4>. URL: <https://www.sciencedirect.com/science/article/pii/B9780128188064000024>.
- [17] Wahyu SETYAWAN and Stefano CURTAROLO. "High-throughput electronic band structure calculations: Challenges and tools". In: *Computational Materials Science* 49.2 (2010), pp. 299–312. ISSN: 0927-0256. DOI: <https://doi.org/10.1016/j.commatsci.2010.05.010>. URL: <https://www.sciencedirect.com/science/article/pii/S0927025610002697>.
- [18] Quan ZHANG et al. "Potential-Driven Semiconductor-to-Metal Transition in Monolayer Transition Metal Dichalcogenides". In: *Advanced Functional Materials* 33 (Oct. 2022). DOI: [10.1002/adfm.202208736](https://doi.org/10.1002/adfm.202208736).
- [19] John P. PERDEW, Kieron BURKE, and Matthias ERNZERHOF. "Generalized Gradient Approximation Made Simple". In: *Phys. Rev. Lett.* 77 (18 Oct. 1996), pp. 3865–3868. DOI: [10.1103/PhysRevLett.77.3865](https://doi.org/10.1103/PhysRevLett.77.3865). URL: <https://link.aps.org/doi/10.1103/PhysRevLett.77.3865>.
- [20] Elliott H. LIEB and Stephen OXFORD. "Improved lower bound on the indirect Coulomb energy". In: *International Journal of Quantum Chemistry* 19.3 (1981), pp. 427–439. DOI: <https://doi.org/10.1002/qua.560190306>. eprint: <https://onlinelibrary.wiley.com/doi/pdf/10.1002/qua.560190306>. URL: <https://onlinelibrary.wiley.com/doi/abs/10.1002/qua.560190306>.
- [21] J.J. MORTENSEN et al. "Bayesian Error Estimation in Density-Functional Theory". In: *Phys. Rev. Lett.* 95 (21 Nov. 2005), p. 216401. DOI: [10.1103/PhysRevLett.95.216401](https://doi.org/10.1103/PhysRevLett.95.216401). URL: <https://link.aps.org/doi/10.1103/PhysRevLett.95.216401>.
- [22] W. KOHN and L. J. SHAM. "Self-Consistent Equations Including Exchange and Correlation Effects". In: *Phys. Rev.* 140 (4A Nov. 1965), A1133–A1138. DOI: [10.1103/PhysRev.140.A1133](https://doi.org/10.1103/PhysRev.140.A1133). URL: <https://link.aps.org/doi/10.1103/PhysRev.140.A1133>.
- [23] Ong Kim LE et al. "Electronic and optical properties of monolayer MoS₂ under the influence of polyethyleneimine adsorption and pressure". In: *RSC Adv.* 10 (8 2020), pp. 4201–4210. DOI: [10.1039/C9RA09042H](https://doi.org/10.1039/C9RA09042H). URL: <http://dx.doi.org/10.1039/C9RA09042H>.
- [24] Xiaolin JIANG et al. "Integrating Density Functional Theory Calculations and Machine Learning to Identify Conduction Band Minimum as a Descriptor for High-Efficiency Hydrogen Evolution Reaction Catalysts in Transition Metal Dichalcogenides". In: *Catalysts* 15.4 (2025). ISSN: 2073-4344. DOI: [10.3390/catal15040309](https://doi.org/10.3390/catal15040309). URL: <https://www.mdpi.com/2073-4344/15/4/309>.
- [25] Lang PENG et al. "Observation of topological states residing at step edges of WTe₂". In: *Nature Communications* 8 (Sept. 2017), p. 65. DOI: [10.1038/s41467-017-00745-8](https://doi.org/10.1038/s41467-017-00745-8).

- [26] Carl NAYLOR et al. “Large-area synthesis of high-quality monolayer 1T'-WTe₂ flakes”. In: *2D Materials* 4 (Feb. 2017), p. 021008. DOI: [10.1088/2053-1583/aa5921](https://doi.org/10.1088/2053-1583/aa5921).
- [27] Andor KORMÁNYOS et al. “k-p theory for two-dimensional transition metal dichalcogenide semiconductors”. In: *2D Materials* 2.2 (Apr. 2015), p. 022001. DOI: [10.1088/2053-1583/2/2/022001](https://doi.org/10.1088/2053-1583/2/2/022001). URL: <https://dx.doi.org/10.1088/2053-1583/2/2/022001>.
- [28] J. J. MORTENSEN, L. B. HANSEN, and K. W. JACOBSEN. “Real-space grid implementation of the projector augmented wave method”. In: *Phys. Rev. B* 71 (3 Jan. 2005), p. 035109. DOI: [10.1103/PhysRevB.71.035109](https://doi.org/10.1103/PhysRevB.71.035109). URL: <https://link.aps.org/doi/10.1103/PhysRevB.71.035109>.
- [29] Alberto GUANDALINI et al. *Efficient GW calculations in two dimensional materials through a stochastic integration of the screened potential*. 2022. arXiv: [2205.11946 \[cond-mat.mtrl-sci\]](https://arxiv.org/abs/2205.11946). URL: <https://arxiv.org/abs/2205.11946>.
- [30] Nicole E. KIRCHNER-HALL et al. “Extensive Benchmarking of DFT+U Calculations for Predicting Band Gaps”. In: *Applied Sciences* 11,5 (2021). ISSN: 2076-3417. URL: <https://www.mdpi.com/2076-3417/11/5/2395>.
- [31] Leonidas MOUCHLIADIS et al. “Probing valley population imbalance in transition metal dichalcogenides via temperature-dependent second harmonic generation imaging”. In: *npj 2D Materials and Applications* 5 (Dec. 2021). DOI: [10.1038/s41699-020-00183-z](https://doi.org/10.1038/s41699-020-00183-z).
- [32] Jussi ENKOVAARA et al. “GPAW - massively parallel electronic structure calculations with Python-based software”. In: *Procedia Computer Science* 4 (2011), pp. 17–25. ISSN: 1877-0509. DOI: <https://doi.org/10.1016/j.procs.2011.04.003>. URL: <https://www.sciencedirect.com/science/article/pii/S1877050911000615>.
Proceedings of the International Conference on Computational Science, ICCS 2011.
- [33] J. ENKOVAARA et al. “Electronic structure calculations with GPAW: A real-space implementation of the projector augmented-wave method”. In: *Journal of physics. Condensed matter: an Institute of Physics journal* 22 (June 2010), p. 253202. DOI: [10.1088/0953-8984/22/25/253202](https://doi.org/10.1088/0953-8984/22/25/253202).
- [34] Jean-Louis CALAIS. “Density-functional theory of atoms and molecules. R.G. Parr and W. Yang, Oxford University Press, New York, Oxford, 1989. IX + 333 pp. Price £45.00”. In: *International Journal of Quantum Chemistry* 47.1 (1993), pp. 101–101. DOI: <https://doi.org/10.1002/qua.560470107>. eprint: <https://onlinelibrary.wiley.com/doi/pdf/10.1002/qua.560470107>. URL: <https://onlinelibrary.wiley.com/doi/abs/10.1002/qua.560470107>.
- [35] John P. PERDEW and Yue WANG. “Accurate and simple analytic representation of the electron-gas correlation energy”. In: *Phys. Rev. B* 45 (23 June 1992), pp. 13244–13249. DOI: [10.1103/PhysRevB.45.13244](https://doi.org/10.1103/PhysRevB.45.13244). URL: <https://link.aps.org/doi/10.1103/PhysRevB.45.13244>.
- [36] Wang YAO, Di XIAO, and Qian NIU. “Valley-dependent optoelectronics from inversion symmetry breaking”. In: *Phys. Rev. B* 77 (23 June 2008), p. 235406. DOI: [10.1103/PhysRevB.77.235406](https://doi.org/10.1103/PhysRevB.77.235406). URL: <https://link.aps.org/doi/10.1103/PhysRevB.77.235406>.
- [37] Weijie ZHAO et al. “Evolution of Electronic Structure in Atomically Thin Sheets of WS₂ and WSe₂”. In: *ACS Nano* 7.1 (2013), pp. 791–797. DOI: [10.1021/nn305275h](https://doi.org/10.1021/nn305275h). eprint: <https://doi.org/10.1021/nn305275h>. URL: <https://doi.org/10.1021/nn305275h>.
PMID: [23256505](https://pubmed.ncbi.nlm.nih.gov/23256505/).

- [38] Ayse BERKDEMIR et al. "Identification of individual and few layers of WS₂ using Raman Spectroscopy". In: *Scientific reports* 3 (Apr. 2013), p. 1755. DOI: [10.1038/srep01755](https://doi.org/10.1038/srep01755).
- [39] R. COEHOORN et al. "Electronic structure of MoSe₂, MoS₂, and WSe₂. I. Band-structure calculations and photoelectron spectroscopy". In: *Phys. Rev. B* 35 (12 Apr. 1987), pp. 6195–6202. DOI: [10.1103/PhysRevB.35.6195](https://doi.org/10.1103/PhysRevB.35.6195). URL: <https://link.aps.org/doi/10.1103/PhysRevB.35.6195>.
- [40] A. KUC, N. ZIBOUCHE, and T. HEINE. "Influence of quantum confinement on the electronic structure of the transition metal sulfide TS₂". English. In: *Physical Review B - Condensed Matter and Materials Physics* 83.24 (June 2011). ISSN: 1098-0121. DOI: [10.1103/PhysRevB.83.245213](https://doi.org/10.1103/PhysRevB.83.245213).
- [41] Andrea SPLENDIANI et al. "Emerging Photoluminescence in Monolayer MoS₂". In: *Nano Letters* 10.4 (2010), pp. 1271–1275. DOI: [10.1021/nl903868w](https://doi.org/10.1021/nl903868w). eprint: <https://doi.org/10.1021/nl903868w>. URL: <https://doi.org/10.1021/nl903868w>. PMID: 20229981.
- [42] Julia GUSAKOVA et al. "Electronic Properties of Bulk and Monolayer TMDs: Theoretical Study Within DFT Framework (GVJ-2e Method)". In: *physica status solidi (a)* 214 (Sept. 2017), p. 1700218. DOI: [10.1002/pssa.201700218](https://doi.org/10.1002/pssa.201700218).
- [43] T. GODDE et al. "Exciton and trion dynamics in atomically thin MoSe₂ and WSe₂: Effect of localization". In: *Phys. Rev. B* 94 (16 Oct. 2016), p. 165301. DOI: [10.1103/PhysRevB.94.165301](https://doi.org/10.1103/PhysRevB.94.165301). URL: <https://link.aps.org/doi/10.1103/PhysRevB.94.165301>.
- [44] Chu QING et al. "Tunable electronic and optical properties of MoTe₂/black phosphorene van der Waals heterostructure: a first-principles study". In: *Physical Chemistry Chemical Physics* 27 (May 2025). DOI: [10.1039/D5CP00675A](https://doi.org/10.1039/D5CP00675A).
- [45] Haihua HUANG et al. "Controlling Phase Transition from Single-Layer MTe₂ (M=Mo, W): Modulation of Potential Barrier under Strain". In: *Phys. Chem. Chem. Phys.* 18 (Jan. 2016). DOI: [10.1039/C5CP06706E](https://doi.org/10.1039/C5CP06706E).
- [46] Rahul Roy. "Topological phases and the quantum spin Hall effect in three dimensions". In: *Phys. Rev. B* 79 (19 May 2009), p. 195322. DOI: [10.1103/PhysRevB.79.195322](https://doi.org/10.1103/PhysRevB.79.195322). URL: <https://link.aps.org/doi/10.1103/PhysRevB.79.195322>.
- [47] Antimo MARRAZZO. "Thermal robustness of the quantum spin Hall phase in monolayer WTe₂". In: *Phys. Rev. Mater.* 7 (2 Feb. 2023), p. L021201. DOI: [10.1103/PhysRevMaterials.7.L021201](https://doi.org/10.1103/PhysRevMaterials.7.L021201). URL: <https://link.aps.org/doi/10.1103/PhysRevMaterials.7.L021201>.
- [48] John P. PERDEW. "Density functional theory and the band gap problem". In: *International Journal of Quantum Chemistry* 28 (1986), pp. 497–523. URL: <https://api.semanticscholar.org/CorpusID:97879042>.
- [49] M. GIANTOMASSI et al. "Electronic properties of interfaces and defects from many-body perturbation theory: Recent developments and applications". In: *physica status solidi (b)* 248.2 (2011), pp. 275–289. DOI: <https://doi.org/10.1002/pssb.201046094>. eprint: <https://onlinelibrary.wiley.com/doi/pdf/10.1002/pssb.201046094>. URL: <https://onlinelibrary.wiley.com/abs/10.1002/pssb.201046094>.